

A New Wave-Front Reconstruction Method for Adaptive Optics Systems Using Wavelets

Peter J. Hampton, *Student Member, IEEE*, Pan Agathoklis, *Senior Member, IEEE*, and Colin Bradley

Abstract—A new technique for wave-front reconstruction from gradient measurements on a square data set is presented. This technique is based on obtaining the Haar wavelet image decomposition of the original wave-front by appropriate filtering and down-sampling of the gradient measurement data. The use of the wavelet decomposition leads to an algorithm with complexity of $O(N)$, where N is the number of data points in the reconstruction, and at the same time allows denoising of the data using the wavelet coefficients. The proposed technique is illustrated with two examples and its reconstruction accuracy, computational speed and denoising performance are discussed. Results indicate that the proposed technique is a computationally efficient and accurate technique for wave-front and/or image reconstruction from gradient measurements.

Index Terms—Adaptive optics, Haar transforms, image reconstruction, wave-front reconstruction.

I. INTRODUCTION

ADAPTIVE OPTICS (AO) systems installed on modern optical telescopes use deformable mirrors (DMs) to correct for aberrations of star light caused by the Earth's atmospheric turbulence [1]. The incoming wave-front is measured by a wave-front sensor (WFS) and this information is used to correct the aberrations with the DM. The Shack-Hartmann WFS (SH-WFS) [2] is one type of sensor used in these systems to measure the gradient of the incoming wave-front at discrete points of a 2-D array, rather than the wave-front shape itself. The reconstruction of the wave-front based on the gradient data is known to satisfy a Poisson partial differential equation [3]. A common approach is to represent the discretized gradient measurements, \vec{s}_x and \vec{s}_y , on the axis of the Cartesian coordinate system given by the following equation [4]:

$$\vec{s} = \begin{bmatrix} \vec{s}_x \\ \vec{s}_y \end{bmatrix} = G \vec{\phi} + \vec{\eta} \quad (1)$$

where $\vec{\phi}$ is the wave-front, $\vec{\eta}$ is the measurement noise and G is a matrix which models the discretized gradient. The commonly used discretizations are Fried [5] and Hudgin [6] models.

Manuscript received February 01, 2008; revised August 01, 2008. Current version published December 10, 2008. This work was supported by the Canada Foundation for Innovation (CFI) and the British Columbia Knowledge Development Fund (BCKDF). The associate editor coordinating the review of this manuscript and approving it for publication was Dr. Julian Christou.

P. J. Hampton and P. Agathoklis are with the Department of Electrical and Computer Engineering, University of Victoria, Victoria, BC, V8W 3P6, Canada (e-mail: peterjhampton@gmail.com; pan@ece.uvic.ca).

C. Bradley is with the Department of Mechanical Engineering, University of Victoria, Victoria, BC, V8W 3P6, Canada (e-mail: cbr@me.uvic.ca).

Digital Object Identifier 10.1109/JSTSP.2008.2006386

There have been several approaches proposed in the literature for solving for $\vec{\phi}$ in (1). The solution using linear algebra is based on converting the 2-D structure into 1-D as in (1) and determining the pseudo-inverse matrix shown in (2) for any G [4]–[6]

$$\vec{\phi}_{\text{estimate}} = (G^T G)^{\dagger} G^T \vec{s}. \quad (2)$$

Such an approach is $O(N^2)$, where N is the number of phase screen pixels for the matrix-vector multiply. This also requires a one time cost of $O(N^3)$ [4] to compute the pseudo-inverse. Wavelet filterbanks have been used to decompose this matrix in an effort to selectively increase the sparseness, reduce complexity of matrix-vector multiplies to $O(N^{3/2})$ and reduce the computation of the pseudo-inverse to $O(N)$ [7].

There are several algorithms that take advantage of fast Fourier transforms to reduce the computational complexity down to $O(N \log N)$. One method developed for the field of computer vision correlates the computed gradients of Gaussian shapes of differing sizes (referred to as “shapelets”) and finds the correlation in the Fourier domain between these shapelets and the gradient measurements to reconstruct the image [8]. Another approach for AO is to determine the solution for Φ in (1) through integrating the gradient data in the Fourier domain and then computing the inverse Fourier transform to obtain the wave-front [9]–[11]. The computation cost is dominated by three Fourier transforms that cost $7.5 N \log_2 N$ in total and some multiple of N flops to combine them [11]. The implementation of the shapelet approach and a basic implementation of Fourier based integration (i.e., with no improvements for application to AO) is available at Kovess's website [12]. The use of the Fourier cosine series has been proposed by Talmi [13] and shown that it converges on a wave-front-estimate in only $19 N$.

Another approach based on the work of Ellerbroek [4] is an iterative method called the multigrid conjugate-gradient (MGCG) method [14]. This method has been shown by Gilles, Ellerbroek, and Vogel in [14] to give an estimate of the wave-front in $28 N \log_2 N$ operations where N is the number of data points that describe the shape of the wave-front on a square. Since then, Gilles has presented an implementation that costs $520 N$ [15] for the required two iterations then Vogel and Yang [3] reduced the computations to $50 N$ for the necessary two iterations. This method takes advantage of the sparseness in the associated matrices, the known statistics of turbulent distortion caused by the atmosphere and performs curvature regularization. This method can also be applied to more complicated problems than discrete Poisson equations, such as multi-conjugate adaptive optics, though at a higher computational cost [3].

There are applications where an image has to be reconstructed from gradient measurement data, such as the camera proposed in [16], where static gradients instead of static intensities are measured and these gradients are used to reconstruct the image. The intent of this system is to reduce saturation of the data by recording the local difference between two pixels rather than the intensity of each pixel. The method proposed in [16] for image reconstruction is based on using a Poisson solver to convert the gradient data to an estimate of the image. One approach to implement a Poisson solver is to begin with the Dirichlet boundary conditions that require measurement of Φ on the boundary. The method chosen in [16] instead solves the boundary condition intensities by adding the given boundary gradient measurement to the estimate of the neighbour point with a starting condition of 0 for the first boundary pixel. Then iteratively solves for the interior points of Φ . Since the boundary data is generally the worst data due to interaction with the pupil edge, applying this approach in AO may lead to errors on the boundary which would propagate to the interior.

In this paper, a new method for open loop wave-front reconstruction from gradient measurement data using wavelets is presented that is $13N$. The approach is based on obtaining the 2-D Haar wavelet decomposition of the original wave-front by filtering and downsampling the gradient measurement data. The filterbanks required for this decomposition are derived directly from the 2-D Haar wavelet analysis filterbank (HWAF) so that the gradient data can be used as input to the filterbank instead of the image data. The original wave-front can then be obtained from this decomposition using a 2-D Haar wavelet synthesis filterbank (HWSF). The use of the wavelet decomposition leads to several benefits with respect to computation complexity, reconstruction accuracy and capability to deal with input measurement noise. The computational complexity of the proposed reconstruction method is of $O(N)$ which is a consequence of using a modification of the discrete wavelet transform (DWT). This solution holds for any scale of data. This is an important property considering that AO optical telescopes currently under development will include a large number of sensor measurement points. The DWT has further the property to “concentrate” most of the energy of the signal in a “small” number of coefficients and thus allow for denoising of the signal using the wavelet coefficients. Since in the first step of the proposed reconstruction technique a wavelet decomposition is generated, these wavelet coefficients can be used to alleviate the effects of any measurement noise in the input. In fact, for signals such as the wave-fronts with aberrations due to atmospheric turbulence which do not contain high frequencies [17], the high frequency part (HH) of the wavelet decomposition can be ignored and thus combine denoising with reduced computations from $13N$ to $8N$.

The paper is organized as follows. In Section II, some general properties of the Haar wavelet decomposition and the notation used are summarized. In Section III the algorithm for reconstruction is presented and its computational complexity is discussed. The proposed technique is illustrated with two examples and its performance is discussed in Section IV. A discussion of the algorithms performance when the gradient model does not

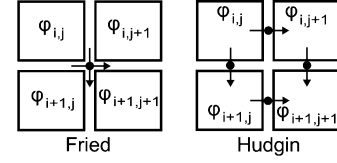


Fig. 1. Fried sensor geometry and Hudgin sensor geometry.

match the sensor as well as suggestions for future work are given in Section V.

II. PRELIMINARIES AND NOTATION

A. Haar Wavelet Filters

The orthogonal Haar filters given by [18]

$$H_L(z) = (1 + z^{-1})/\sqrt{2} \quad (3)$$

$$H_H(z) = (1 - z^{-1})/\sqrt{2} \quad (4)$$

can be used to obtain decompositions of data by filtering in either the vertical or horizontal directions. To distinguish between these directions, z_h will indicate horizontal filtering of rows whereas z_v will indicate vertical filtering of columns.

B. Sensor Geometries

Consider the case where the vertical and the horizontal gradients of the image intensity are available and the objective is to reconstruct the original image from the available gradient information. In AO, two different geometries have been used to represent the gradient data. Using the notation of [9], they are the Hudgin geometry [6] and the Fried geometry [5].

Using the Hudgin geometry in Fig. 1, the difference between two points is sensed and the gradient data is

$$H\tilde{x}_{i,j} = -\varphi_{i,j} + \varphi_{i,j+1} \quad (5)$$

$$H\tilde{y}_{i,j} = -\varphi_{i,j} + \varphi_{i+1,j}. \quad (6)$$

Thus, the horizontal and vertical gradients of an image $^M\Phi$ of size $2^M \times 2^M$, using the Hudgin geometry can be represented as matrices $^M_H\tilde{X}$ and $^M_H\tilde{Y}$ respectively and will be of size $2^M \times (2^M - 1)$ and $(2^M - 1) \times 2^M$, respectively. This nonsquare structure is the result of filtering $^M\Phi$ in only one direction for each of the gradient directions.

Using the Fried geometry in Fig. 1, the sensor measurement is made in the center of a square of four grid points. This is the average of two Hudgin aligned sensors. This is represented by the following two equations for each individual sensor:

$$\begin{aligned} F\tilde{x}_{i,j} &= 0.5(H\tilde{x}_{i,j} + H\tilde{x}_{i+1,j}) \\ &= 0.5(-\varphi_{i,j} + \varphi_{i,j+1} - \varphi_{i+1,j} + \varphi_{i+1,j+1}) \end{aligned} \quad (7)$$

$$\begin{aligned} F\tilde{y}_{i,j} &= 0.5(H\tilde{y}_{i,j} + H\tilde{y}_{i,j+1}) \\ &= 0.5(-\varphi_{i,j} - \varphi_{i,j+1} + \varphi_{i+1,j} + \varphi_{i+1,j+1}). \end{aligned} \quad (8)$$

The horizontal and vertical gradients of an image $^M\Phi$, using the Fried geometry, can then be represented as matrices $^M_F\tilde{X}$ and $^M_F\tilde{Y}$ respectively and will be of size $(2^M - 1) \times (2^M - 1)$. The relationship between the gradient measurements obtained using

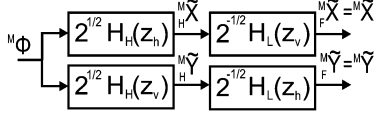


Fig. 2. Relationship between Hudgin and Fried aligned gradient models.

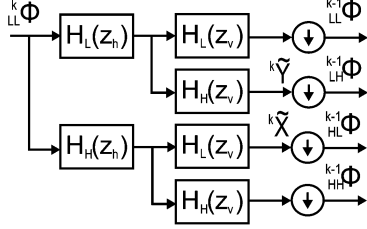


Fig. 3. One stage of the HWAF. Stages cascade by connecting the LL output to the LL input of the next stage.

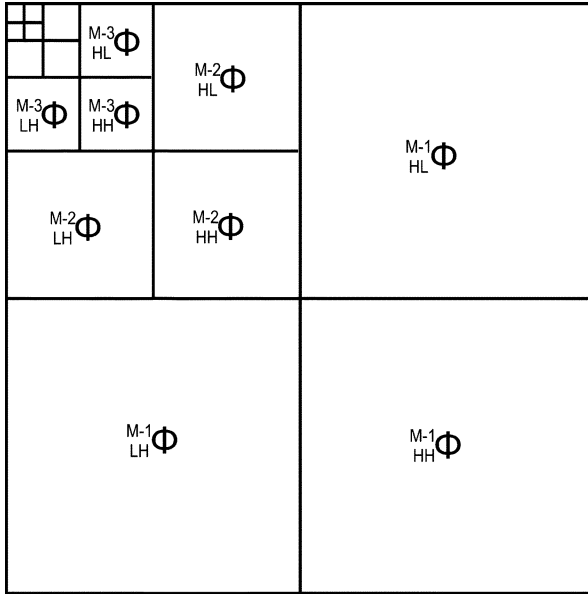


Fig. 4. Image decomposition using a HWAF.

these two geometries can be represented by the Haar filters and are shown in Fig. 2 and (9) and (10)

$$M\tilde{X} = \frac{M}{F}\tilde{X} = \frac{M}{H}\tilde{X}H_L(z_v) = M\Phi H_H(z_h)H_L(z_v) \quad (9)$$

$$M\tilde{Y} = \frac{M}{F}\tilde{Y} = \frac{M}{H}\tilde{Y}H_L(z_h) = M\Phi H_L(z_h)H_H(z_v). \quad (10)$$

C. Haar Wavelet Filterbanks

The structure of one stage of the 2-D HWAF is shown in Fig. 3. Let the symbol $\tilde{\Phi}$ represent a 2-D image. The superscript to the top left of $k\tilde{\Phi}$ indicates the stage and also the size of the 2-D image, i.e., $k\tilde{\Phi}$ is of size $2^k \times 2^k$ for $k = 1 \leq k \leq M$. The subscripts LL, LH, HL and HH introduced in Fig. 3 indicate the

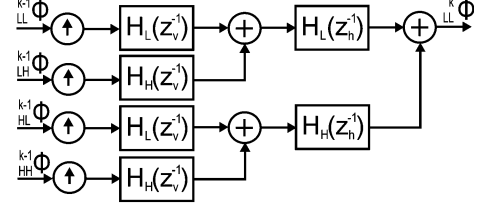


Fig. 5. Structure of HWSF. Stages cascade by connecting the LL output to the LL input of the next stage.

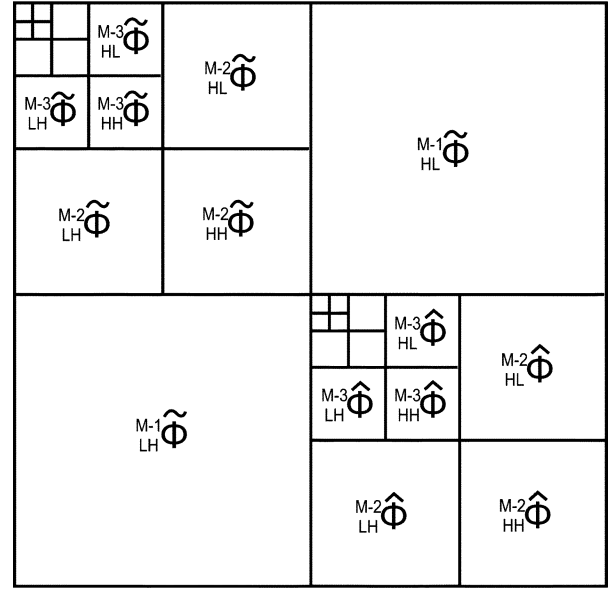


Fig. 6. Image decomposition obtained from gradient data.

order that the Haar filters were applied to the signal. By cascading wavelet filter blocks such as the one in Fig. 3 to each LL output, an M-stage 2-D filterbank is obtained where the output of the last stage is a block of 2×2 pixels. This M-stage HWAF leads to the decomposition of Fig. 4.

Using the equivalent analysis filters for M-stage 2-D filterbanks, the nonrecursive structure of the Haar wavelet decomposition of the image can be obtained as

$$\begin{aligned} M_{LL}^{-m}\Phi &= \downarrow_{2^m} \left\{ M\Phi \prod_{k=0}^{m-1} H_L(z_h^{2^k}) \prod_{k=0}^{m-1} H_L(z_v^{2^k}) \right\} \end{aligned} \quad (11)$$

$$\begin{aligned} M_{LH}^{-m}\Phi &= \downarrow_{2^m} \left\{ M\Phi H_H(z_v^{2^{m-1}}) \prod_{k=0}^{m-1} H_L(z_h^{2^k}) \prod_{k=0}^{m-2} H_L(z_v^{2^k}) \right\} \end{aligned} \quad (12)$$

$$\begin{aligned} M_{HL}^{-m}\Phi &= \downarrow_{2^m} \left\{ M\Phi H_H(z_h^{2^{m-1}}) \prod_{k=0}^{m-2} H_L(z_h^{2^k}) \prod_{k=0}^{m-1} H_L(z_v^{2^k}) \right\} \end{aligned} \quad (13)$$

$$\begin{aligned} M_{HH}^{-m}\Phi &= \downarrow_{2^m} \left\{ M\Phi H_H(z_h^{2^{m-1}}) H_H(z_v^{2^{m-1}}) \cdots \right. \\ &\quad \left. \cdots \prod_{k=0}^{m-2} H_L(z_h^{2^k}) \prod_{k=0}^{m-2} H_L(z_v^{2^k}) \right\} \end{aligned} \quad (14)$$

where $\downarrow_k \{ \}$ is the down sampling function in both horizontal and vertical directions by the factor k . The first valid data point of filtering is where the data fully supported the filter. Down-sampling by two retains data points on odd columns and rows.

In this paper, the structure of the HWAF given by (11) to (14) will be modified by rearranging the order of operations to allow for image gradient data to be used as the input for the decomposition. The original image can then be reconstructed by applying a standard HWSF to the image decomposition, i.e., the decomposition provided by the HWAF is perfectly reversible by the HWSF as in Fig. 5.

III. HAAR DECOMPOSITION FROM GRADIENT DATA

The approach for wave-front reconstruction presented in this section is based on generating the decomposition given in Fig. 6, from $^M\tilde{X}$ and $^M\tilde{Y}$, (9) and (10), and then obtain the original wave-front using standard HWSFs applied to this decomposition.

The motivation for developing the decomposition of Fig. 6 is based on the similarity between the Haar wavelet and the representation of the gradient measurements using the Fried model. Comparing Fig. 2 to Fig. 3 it is clear that gradient data that matches the Fried model perfectly provides the filtering necessary to obtain $^{M-1}_{LH}\tilde{\Phi}$ and $^{M-1}_{HL}\tilde{\Phi}$. All that is required is down-sampling of the measurements to obtain the upper-right and lower-left part of the decomposition shown in Fig. 4. Obtaining the diagonal sections of Fig. 6 using the gradient data requires the development of filterbanks which are no more than a manipulation of the order of operations of the linear filters in the HWAF and the HWSF. The algebraic proof is provided in the Appendix. This manipulation can be considered as converting the Haar decomposition from a denoising/compression tool into an important intermediate step when solving 2-D discrete partial differential equations.

A. Reconstruction Algorithm

The reconstruction of the original wave-front is obtained in two steps, the *Analysis* and the *Synthesis* steps. The filterbank for the first three quadrants of Fig. 6 is given as Fig. 7.

Analysis Step: Given $^M\tilde{X}$ and $^M\tilde{Y}$, in (9) and (10), generate the decomposition of Fig. 6:

HL and LH quadrants (upper right and lower left quadrants)

$$^{M-1}_{HL}\tilde{\Phi} = \downarrow_2 \{ ^M\tilde{\Phi} H_H(z_h) H_L(z_v) \} = \downarrow_2 \{ ^M\tilde{X} \} \quad (15)$$

$$^{M-1}_{LH}\tilde{\Phi} = \downarrow_2 \{ ^M\tilde{\Phi} H_L(z_h) H_H(z_v) \} = \downarrow_2 \{ ^M\tilde{Y} \} \quad (16)$$

LL quadrant (upper left quadrant of Fig. 6)

For $k = M$ to 2

$$^{k-1}\tilde{Y} = \sqrt{2} \downarrow_2 \{ ^k\tilde{Y} H_L(z_h^2) H_L^2(z_v^2) \} \quad (17)$$

$$^{k-1}\tilde{X} = \sqrt{2} \downarrow_2 \{ ^k\tilde{X} H_L^2(z_h^2) H_L(z_v^2) \} \quad (18)$$

$$^{k-2}_{LH}\tilde{\Phi} = \downarrow_2 \{ ^{k-1}\tilde{Y} \} \quad (19)$$

$$^{k-2}_{HL}\tilde{\Phi} = \downarrow_2 \{ ^{k-1}\tilde{X} \} \quad (20)$$

$$\begin{aligned} ^{k-2}_{HH}\tilde{\Phi} &= \sqrt{2} \downarrow_4 \{ ^k\tilde{Y} H_H(z_h^2) H_L^2(z_v^2) \} \\ &= \sqrt{2} \downarrow_4 \{ ^k\tilde{X} H_L^2(z_h^2) H_H(z_v^2) \} \end{aligned} \quad (21)$$

end

$$^{0}_{LL}\tilde{\Phi} = 2^M \text{mean}(\Phi) \quad (22)$$

i.e., $^{0}_{LL}\tilde{\Phi}$ is proportional to the mean value of the image.

HH quadrant (lower right quadrant of Fig. 6):

For $k = M$ to 2

$$^{k-1}\hat{X} = \begin{cases} \sqrt{2} \downarrow_2 \{ ^M\tilde{X} H_L(z_h^2) H_H^2(z_v^2) \}, & \text{for } k = M \\ \sqrt{2} \downarrow_2 \{ ^k\hat{X} H_L(z_h^2) H_L^2(z_v^2) \}, & \text{for } k < M \end{cases} \quad (23)$$

$$^{k-1}\hat{Y} = \begin{cases} \sqrt{2} \downarrow_2 \{ ^M\tilde{Y} H_H^2(z_h^2) H_L(z_v^2) \}, & \text{for } k = M \\ \sqrt{2} \downarrow_2 \{ ^k\hat{Y} H_L^2(z_h^2) H_L(z_v^2) \}, & \text{for } k < M \end{cases} \quad (24)$$

$$^{k-2}_{LH}\hat{\Phi} = \downarrow_2 \{ ^{k-1}\hat{X} \} \quad (25)$$

$$^{k-2}_{HL}\hat{\Phi} = \downarrow_2 \{ ^{k-1}\hat{Y} \} \quad (26)$$

$$\begin{aligned} ^{k-2}_{HH}\hat{\Phi} &= \begin{cases} \sqrt{2} \downarrow_4 \{ ^M\tilde{Y} H_H^2(z_h^2) H_H(z_v^2) \}, & \text{for } k = M \\ \sqrt{2} \downarrow_4 \{ ^k\hat{Y} H_L^2(z_h^2) H_H(z_v^2) \}, & \text{for } k < M \end{cases} \\ &= \begin{cases} \sqrt{2} \downarrow_4 \{ ^M\tilde{X} H_H(z_h^2) H_H^2(z_v^2) \}, & \text{for } k = M \\ \sqrt{2} \downarrow_4 \{ ^k\hat{X} H_H(z_h^2) H_L^2(z_v^2) \}, & \text{for } k < M \end{cases} \end{aligned} \quad (27)$$

end

Synthesis Step: Given the image decomposition of Fig. 6 obtained in the Analysis step:

Apply an M-1-stage HWSF to HH quadrant to obtain $^{M-1}_{HH}\tilde{\Phi}$.

Apply an M-stage HWSF to all 4 quadrants, including $^{M-1}_{HH}\tilde{\Phi}$, to obtain the wave-front estimate.

Algorithm end.

The above equations have been obtained by combining (9) or (10) with (12)–(14) to obtain the wavelet decomposition given in Fig. 6 from the gradient signals $^M\tilde{X}$ and $^M\tilde{Y}$, instead of the image, $^M\Phi$, as input (see the Appendix).

There are two entries in the decomposition given in Fig. 6 which cannot be obtained from the gradient data. The first is $^{0}_{LL}\tilde{\Phi}$ which is the mean of the image and could be found with an additional sensor to measure the mean as suggested in (22). In AO, the mean is called piston and it may be acceptable that this value would be set to 0. In other applications, such as the one considered in example 2, $^{0}_{LL}\tilde{\Phi}$ can be estimated from the knowledge of the signal dynamic range.

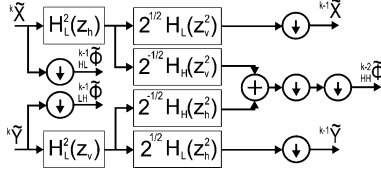


Fig. 7. Gradient analysis filterbank structure for HL, LH and LL quadrants.

The other entry is ${}^0_{LL}\hat{\Phi}$. The HH quadrant represented by ${}^{M-1}_{HH}\Phi$ in Fig. 4 is entirely composed of 2×2 waffle, just as ${}^{M-1}_{LH}\Phi$ and ${}^{M-1}_{HL}\Phi$ are 2×2 tilts and ${}^{M-1}_{LL}\Phi$ is 2×2 pistons. Any waffle-type shape is composed of linear combinations of these 2×2 waffle modes. However, ${}^{M-1}_{HH}\Phi$ cannot be solved directly because it contains one invisible waffle shape. This mode is proportional to a checkerboard pattern given as $(-1)^{i+j}$, where i and j represent the row and column of the image. It was determined that the invisible component of ${}^{M-1}_{HH}\Phi$ can be isolated by applying an M-1 stage HWAF to ${}^{M-1}_{HH}\Phi$. This allows the other visible components to be solved directly. The magnitude of invisible waffle is directly proportional to ${}^0_{LL}\hat{\Phi}$. As suggested by the subscripts, it is directly proportional to the mean value of all the 2×2 waffle modes that compose ${}^{M-1}_{HH}\Phi$. Such a high-frequency component is known to be unusable in AO and is also expected to not have a significant magnitude in digital photography. This is supported by the small reconstruction error found in Section IV. Therefore, ${}^0_{LL}\hat{\Phi}$ can be set to 0 and ignored without significant error.

Further, it is known from atmospheric turbulence models that the high spatial frequency shapes are reduced by a factor of $f^{-11/3}$ in power as spatial frequency increases [17], which makes the signal-to-noise ratio (SNR) poor at high frequencies. It can be desirable to remove the localized waffle from the corrected modes [19]. The Haar decomposition automatically isolates compactly supported waffle modes into the HH quadrant. This allows for removal of these modes simply by not computing the respective portion of the decomposition. This is only shown for the open loop case in the example section and has yet to be proven to be suitable for closed loop operation.

B. Computational Complexity

The computational complexity of the proposed algorithm can be established based on the complexity of the 2-D separable DWT [18]. Both the Analysis and Synthesis steps of the proposed algorithm involve convolutions with separable wavelet filters followed by down-sampling in both dimensions and thus, based on [18], the computational complexity will be of order $O(N)$, where $N = 2^M \times 2^M$. Thus, the proposed algorithm is scaling linear with the number of sensors.

The constant coefficient before the linear term N depends on the type of filters used and on the implementation. An upper limit for the complexity of the proposed algorithm can be found by considering that the convolution of $H_L(z)$ or $H_H(z)$, (3) and (4), with a matrix containing N total elements requires approximately $3N$ operations and similarly, the convolution of $H_L(z)H_L(z)$ with N data points is $5N$ operations. Taking advantage of down-sampling, each of ${}^{M-2}_{HL}\hat{\Phi}$, ${}^{M-2}_{LH}\hat{\Phi}$, ${}^{M-2}_{HL}\hat{\Phi}$ and ${}^{M-2}_{LH}\hat{\Phi}$ would require $3.25N$ operations. Since ${}^{M-2}_{HH}\hat{\Phi}$ and

${}^{M-2}_{HH}\hat{\Phi}$ can be computed from either ${}^M\tilde{X}$ or ${}^M\tilde{Y}$, the average of the two is used with a cost of $6.625N$ for each of these sections. Each subsequent value of m operates on one quarter less data than the previous stage leading to the following complexity for the analysis step:

$$C_{\text{Analysis}}(N) \leq (4 * 3.25 + 2 * 6.625)N \sum_{k=0}^{M-2} \frac{1}{4^k} \leq 26.25N \left(\frac{4}{3} \right) = 35N. \quad (28)$$

In the synthesis step, the HWSF used to reconstruct the M-1 stages of the HH quadrant requires N operations and the reconstruction of the M stages requires an additional $4N$. This leads to a $C_{\text{Synthesis}}(N)$ of $5N$ and a total complexity for the reconstruction of

$$C_{\text{Total}}(N) = C_{\text{Analysis}}(N) + C_{\text{Synthesis}}(N) \leq 40N. \quad (29)$$

$C_{\text{Analysis}}(N)$ is the upper bound for the complexity of the analysis step using $H_L(z)$ and $H_H(z)$. By taking into consideration the special values of the coefficients of $H_L(z)$ and $H_H(z)$ and avoiding redundant computations to compute ${}^{M-2}_{HH}\hat{\Phi}$ and ${}^{M-2}_{HH}\hat{\Phi}$, as is done in the implementation used in the experiments, the complexity of the analysis step is reduced to approximately $8N$ and the total complexity to $13N$.

Remark: The proposed technique has been developed using a rectangular grid of gradient measurements. In most astronomical AO systems, the gradients are available on a circular grid, not on a rectangular grid. Extending circular aperture measurements to rectangular measurements by zero padding leads to errors. Instead the extension has to be carried out in a way that takes care of the boundary. By using the discrete partial differentiation model, the extrapolation can be performed by choosing the exterior values such that the integral of gradient measurements on any closed path must be zero [9] in the absence of noise. The solution varies depending on the assumptions made of the exterior region. Assumptions shown in the literature are to assume the field goes to zero after a transition period [9], maintains periodicity [10] or that the mean of the interior and exterior are each zero [13]. The filterbank developed in this paper could also operate on these extended data sets. Since in this paper the focus is on introducing this new filterbank structure, its quality of reconstruction and computation speed, the extension to circular apertures will be discussed in subsequent publications.

The performance of the proposed algorithm will be illustrated and evaluated in the next section.

IV. EXAMPLES

In this section, the proposed technique is illustrated and its performance is evaluated using two experiments. In the first one, a square wave-front is reconstructed based on measurements using the Fried model as the SH-WFS. The second is an example of reconstruction of a photograph from Hudgin aligned numerical measurements of its gradient data. These are to demonstrate performance when the sensor matches these models perfectly. A discussion on modeling error follows this section.

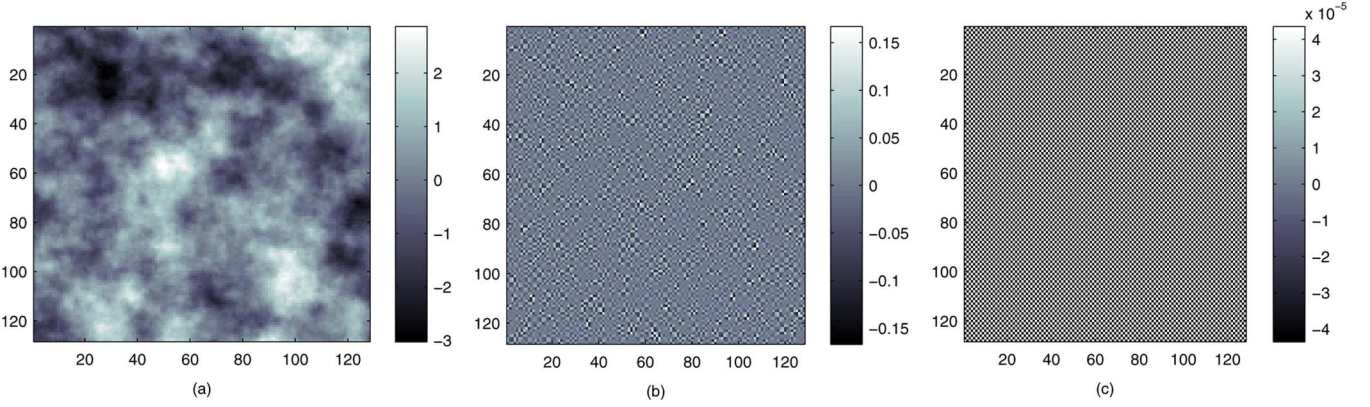


Fig. 8. (a) Reconstructed wave-front; (b) residual error when HH quadrant is suppressed; (c) residual error from full reconstruction.

A. Atmospheric Phase Screen Reconstruction

To evaluate the performance of the proposed algorithm for wave-front reconstruction, atmospheric phase screens are generated using a Kolmogorov turbulence model with r_0 of 0.25 m, wavelength of 500 nm, pupil diameter of 32 m, and outer scale of 22 m. These are the same parameters as in [3] with the exception of the outer scale which was not given in [3] and was chosen based on measurements at the Paranal ESO observatory in Chile [20]. The phase screen generation software was developed according to the discussion in [21]. The gradient data ($^M\tilde{X}$ and $^M\tilde{Y}$) are obtained by using a simulated sensor that uses the Fried aligned operators of (7) and (8). The phase screen is 128×128 so that the Fried sensor model will provide two 127×127 sets of data.

The phase screen is reconstructed using the proposed technique based on the simulated sensor data contaminated, where appropriate, with Gaussian white noise. The input SNR is obtained using $^M\tilde{X}$ and $^M\tilde{Y}$ as the signal similarly to [3]. To evaluate the capacity of the algorithm to remove high frequency waffle, two reconstructions are produced for each test. The first is based on using the full decomposition of Fig. 6, while in the second, the HH quadrant is suppressed (i.e., equating all entries of $^M\tilde{\Phi}_{HH}$ to zero). The quality of the reconstruction is evaluated using the rms normalized residual error of the pixels of a single phase screen calculated by

$$E_R = \frac{\| \Phi_{\text{Reconstructed}} - \Phi_{\text{Original}} \|}{\| \Phi_{\text{Original}} \|} \quad (30)$$

as well as the 66 Zernike modes (corresponding up to radial order 10) of a largest inner circle inside the 128×128 phase screen [17].

In the first part of this experiment, the phase screen was reconstructed assuming no measurement noise. The full wave-front reconstruction using the proposed algorithm is shown in Fig. 8(a). There is no visible difference between the full reconstruction and the reconstruction with neglected HH (and thus it is not included here). The error for the full reconstruction is shown in Fig. 8(c) and is only composed of a pure checkerboard pattern corresponding to the $^0_{LL}\hat{\Phi}$ entry in the decomposition of Fig. 6. This entry is invisible to the sensor and the algorithm does not attempt to reconstruct this shape, just as it does not reconstruct the mean value. E_R for the full reconstruction is 0.000503

rms where the amplitude of the phase screen is normalized to 1 rms.

The error for the reconstruction neglecting HH is given in Fig. 8(b) and the corresponding E_R is 0.0383 rms. The Zernike coefficients for the original phase screen are shown in Fig. 9(a) and the Zernike coefficients of the reconstruction error for the two reconstructions are shown in Fig. 9(b). The low reconstruction error and the low relative magnitude of the Zernike coefficients of the reconstruction error indicate excellent reconstruction. Further, when there is no measurement noise, the full reconstruction gives better results.

In the second part of this experiment, Gaussian white measurement noise with $\text{SNR} = 20$ (i.e., 26 dB) is added to the gradient data and the phase screen is reconstructed from the noisy gradient data as in [3]. The E_R for the full reconstruction is 0.0232 rms and the reconstruction neglecting HH is 0.0495 rms. Further, the Zernike coefficients of the reconstruction error for the full reconstruction and the reconstruction neglecting HH are shown in Fig. 9(c). For comparison, the Zernike coefficients of the reconstruction error obtained from directly projecting the gradient data to Zernike modes are shown as the dark line. For the 66 modes shown, the rms of the Zernike coefficients of the reconstruction error is only ~ 1.5 times larger than the rms of the Zernike coefficients of the measurement noise.

To further evaluate the performance of the proposed algorithm in the presence of measurement noise, a series of reconstructions using noisy gradient data with several values of SNR were performed for both the full reconstruction and the reconstruction neglecting HH. The results with respect to the normalized residual error are presented in Fig. 10.

To evaluate the computational complexity of the proposed method and the effect of neglecting the HH quadrant on the computational speed, wave-fronts of various resolutions were generated and the computation times are given as Fig. 11. This shows that the computation time is linear with the number of pixels for large numbers of pixels. It also shows that the algorithm requires at least a 128×128 reconstruction for the computation time to be significant compared to MatLab's overhead because the time per pixel is significantly decreasing until that size. These computations were made using MatLab and thus the computation times are not indicative of computation time in a real-time implementation.

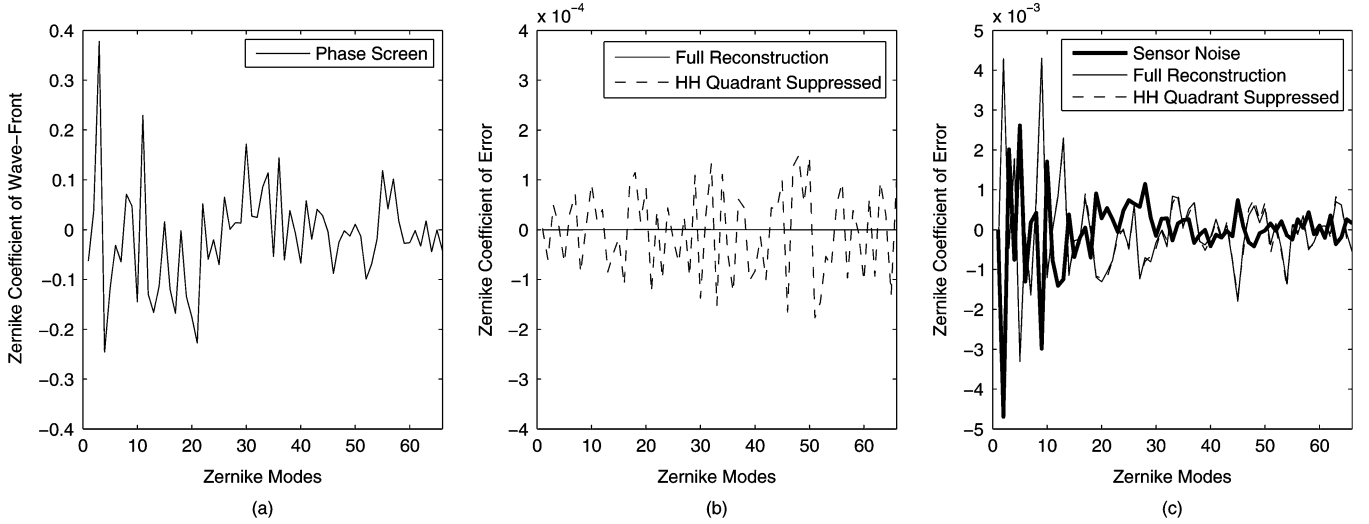


Fig. 9. Zernike coefficients of (a) wave-front, (b) error with $\text{SNR} = \infty$, and (c) error with $\text{SNR} = 20$.

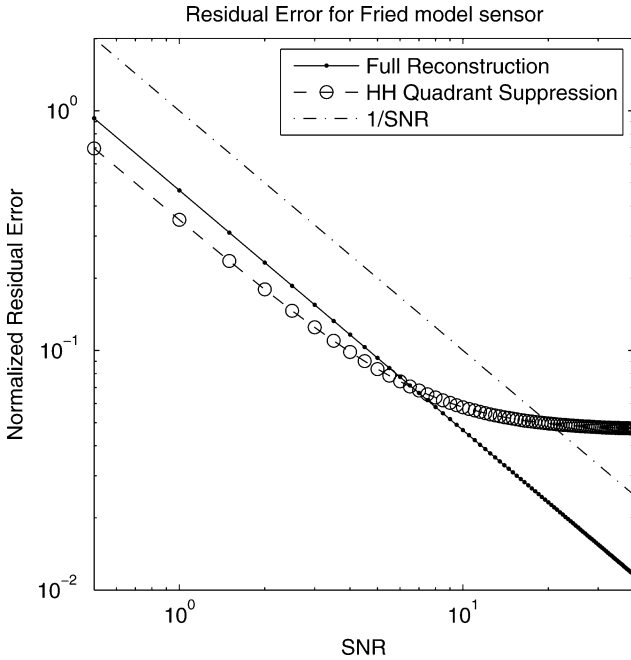


Fig. 10. Reconstruction error compared to the inverse of the SNR.

Remark: For AO examples, $\tilde{\Phi}_{LL}^0$ has been assumed to be zero. The assumption of $\tilde{\Phi}_{LL}^0$ equal to zero is accurate since the simulated wave-front has a mean of zero. In AO, the mean does not contribute to the error of wave-front correction so its actual value is irrelevant.

B. Photograph Reconstruction

A 2048×2048 image is being considered and the Hudgin aligned gradient data, \tilde{X}_H^M and \tilde{Y}_H^M , are obtained using (5) and (6). The Hudgin model measures the difference between two neighbour pixels in the horizontal and vertical directions. The proposed algorithm can solve for the original data by first converting this data to Fried aligned data as in (9) and (10).

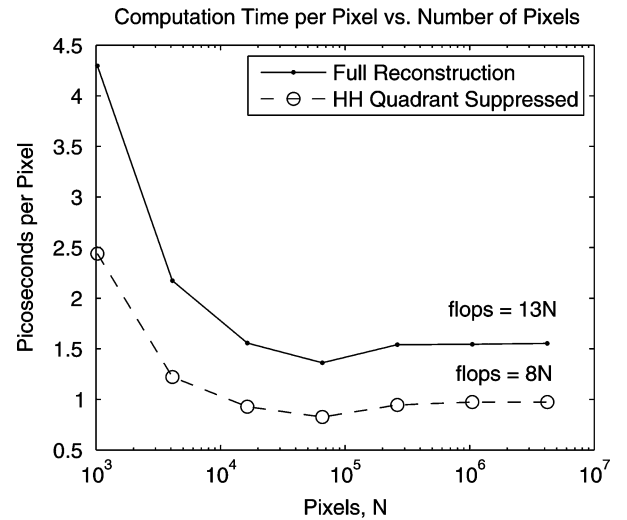


Fig. 11. Computation time per pixel in MatLab implementation.

Atmospheric turbulence follows a known statistical model. In general, photographs do not. This experiment shows the algorithms performance when solving discrete partial differential equations for unknown statistics of the data.

The image is reconstructed from noiseless gradient data using the proposed technique. The full reconstruction of the 8-bit image is perfect after rounding to integer values.

Fig. 12 shows the error when the data from the HH quadrant, i.e., $\tilde{\Phi}_{HH}^{M-1}$, is not computed. The dynamic range of this error is about 88 (compared to 255 dynamic range of image). However, the rms of the reconstruction error when ignoring the HH quadrant is only -31 dB (0.028 rms).

To illustrate the effect of noise, the reconstruction of the above image is carried out using noisy gradient data. In Fig. 13, the reconstructed image using the proposed technique is shown for the case when the SNR of the noisy gradient data is 6 dB (i.e., $\text{SNR} = 2$). The reconstruction error in Fig. 13 is -20.3

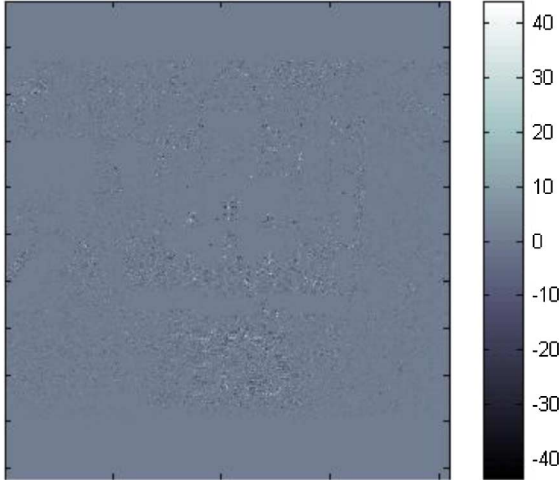


Fig. 12. Reconstruction error from suppressing the HH quadrant.

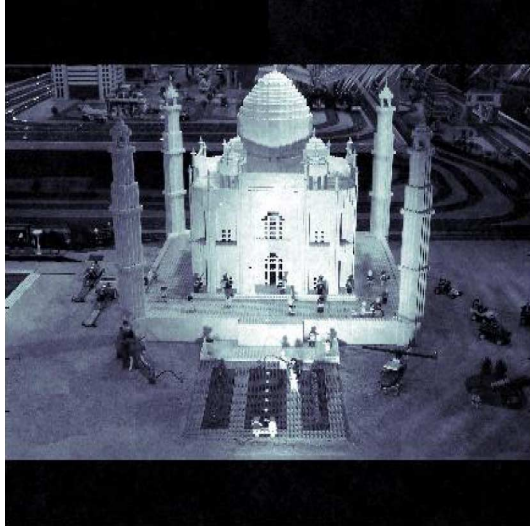


Fig. 13. Reconstruction from gradient data corrupted to $\text{SNR} = 2$ (or 6 dB).

dB (0.095 rms). This is a visually acceptable reconstruction despite significant input noise.

Measurement noise does have a significant effect on the quality of the estimate of data in the HH quadrant. Fig. 14 shows the SNR of the gradient data used as input and the SNR of the reconstruction error for both cases: full reconstruction and reconstruction while neglecting the HH quadrant. The full reconstruction error is shown to be -14.3 dB smaller than the inverse of the SNR. This means that the ratio of the reconstructed image to the reconstructed error is 5.2 times greater than the input signal to noise ratio. This result is independent of any denoising techniques that could be applied.

It can be seen from Fig. 14 that when the input SNR is reduced to about 3, the $\hat{\Phi}_{HH}^{M-1}$ estimate becomes corrupted and the full reconstruction does not give lower reconstruction error than the reconstruction neglecting the HH quadrant.

Remark: In this example, the mean value is assumed not known and was set to zero for reconstruction. The reconstruction has a dynamic range of -75.959 to 179.041 . Since the original image is an 8-bit image and coincidentally used the full 0 to

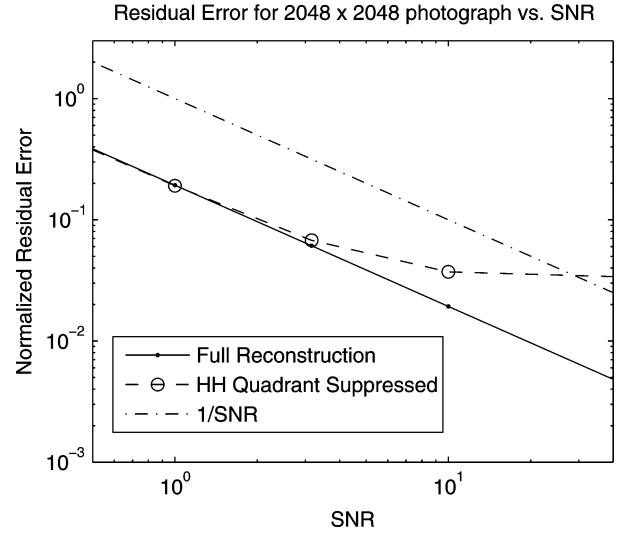


Fig. 14. Reconstruction error for the 2048×2048 photograph versus SNR.

255 dynamic range, this implies that the mean should be chosen to be 75.959. However, the reported error ignores mean value error.

V. DISCUSSION

These examples indicate that the proposed reconstruction technique is a fast and efficient method to reconstruct simulated wave-fronts and/or images from gradient data when the application model matches the Hudgin or Fried models. By applying the method to photographs and to atmospheric turbulence models, it shows that the reconstruction is not dependant on assumed statistical properties of the data. For the 128×128 case, the full reconstruction improved the SNR by a factor of approximately two as opposed to approximately five for the 2048×2048 case. This suggests that noise rejection may improve as the data sets get larger and may help mitigate the effect of dividing the number of collected photons between more sensor points.

An important consideration is to determine how well the algorithm performs when the model does not match the sensor. The Fried model is only an approximation to how a real SH-WFS would operate. Naturally, reconstruction errors are introduced when the Fried sensor model does not match the SH-WFS and there are other forms of WFSs such as [22].

The proposed algorithm was also operated on an alternate model of the SH-WFS. This model was used by Vogel and Yang [3] that takes a 4×4 block of phase screen pixels and determines the average slope in the horizontal and vertical directions. Due to mathematical canceling from numerical integration of the difference of pixels, our interpretation of this sensor is given as (31) and (32)

$$x_{p,q} = \frac{1}{3} \sum_i \sum_k \begin{bmatrix} -\phi_{i,k} & 0 & 0 & \phi_{i,k+3} \\ -\phi_{i+1,k} & 0 & 0 & \phi_{i+1,k+3} \\ -\phi_{i+2,k} & 0 & 0 & \phi_{i+2,k+3} \\ -\phi_{i+3,k} & 0 & 0 & \phi_{i+3,k+3} \end{bmatrix} \quad (31)$$

$$y_{p,q}$$

$$= \frac{1}{3} \sum_i \sum_k \begin{bmatrix} -\phi_{i,k} & -\phi_{i,k+1} & -\phi_{i,k+2} & -\phi_{i,k+3} \\ 0 & 0 & 0 & 0 \\ 0 & 0 & 0 & 0 \\ \phi_{i+3,k} & \phi_{i+3,k+1} & \phi_{i+3,k+2} & \phi_{i+3,k+3} \end{bmatrix} \quad (32)$$

where p and q are the row and column of the measurement point on the sensor grid and $i = 4p - 1$ and $k = 4q - 1$ are the row and column representing the top corner of the respective 4×4 cell of the phase screen. The indices i and k were chosen so that a 512×512 phase screen would generate 127×127 sensor grid points to sense 128×128 blocks in Fried alignment.

This shows that alternate valid SH-WFS models may be very different than the assumed Fried model. The main issue that makes this model different from the Fried model is the Fried model would consist of two sets of 16×16 nonzero weighting factors. This alternate model has weighting from only 8 pixels for each direction and thus this model only uses 12.5% of the area of support of the Fried model. The gradient data generated by both methods were calculated for the same phase screen and it was determined that the difference between the two data sets was 0.416 rms, normalized to the ideal Fried measurements. This modeling error is similar to $\text{SNR} = 2.4$, though it is dependent on the phase screen itself and is not a random signal.

Gradient measurements were generated by (31) and (32) for a 127×127 sensor grid. Even with these large modeling errors that are not independent of the signal, the full reconstruction generated using the proposed algorithm had 0.136 rms reconstruction error. The reconstruction neglecting the HH component, resulted in a reduced error of 0.081 rms. For comparison, these relative errors are consistent with the results shown in Fig. 10 for a SNR value of about 3.

To improve the reconstruction using the proposed algorithm in the case of model mismatch, a simple low-pass filter was applied to the gradient data using the alternate model. This low-pass filtering reduced the difference between the gradient data from the alternate model and the Fried model to 0.227 rms (from 0.416 rms in the previous experiment). Using the filtered data, the full reconstruction resulted in an error of 0.055 rms and the reconstruction neglecting HH in an error of 0.060 rms. For comparison, in [3] using the MGCG for bicubic influence functions, the reconstruction solution error was improved from 0.20 rms to less than 0.01 rms by using curvature regularization. Similarly, the performance of the proposed algorithm in the presence of the gradient model mismatch is expected to improve by reducing the effects of model mismatch. Since even a simple low pass filter improved the results, it is expected that implementing filters minimizing the curvature error, such as in MGCG, would further improve results. Curvature regularization must be explicitly implemented in order to be a least-squares solution.

Another area of possible improvement of the proposed algorithm is the use of wavelets to denoise a wave-front using Fig. 4 as shown by Donoho [23] instead of simply eliminating the HH part. As was shown in Section 3, an intermediate step for solving for the wave-front in the proposed algorithm is the Haar wavelet decomposition. Therefore, denoising techniques could be performed at this stage [23] before proceeding to the final estimate to alleviate the effects of measurement noise in the input.

An alternate approach to denoising suggested by Kolaczky is to threshold the noise based on the Poisson nature of photon noise [24].

Finally, AO systems operate on gradient data that have circular support. It has been shown in the literature [9], [10], [13] that gradient data with circular support can be extrapolated to a square for use with the square Fourier transform and Fourier series based reconstruction methods. It is an important area of research to prove that this method works with extrapolation.

VI. CONCLUSION

A new technique for wave-front reconstruction from gradient measurements with square support is presented. This technique is based on obtaining the Haar wavelet image decomposition of the original wave-front by appropriate filtering and down-sampling of the gradient measurement data. The filters required for filtering are obtained by modifying the standard 2-D Haar filterbanks to use gradient data instead of image data as input. The use of the wavelet decomposition leads to an algorithm shown to be of complexity of $O(N)$, where N is the number of data points in the square reconstruction. It is asserted that this can be implemented in $13N$ for full reconstruction and as few as $8N$ when disregarding the high frequency components. An added benefit of using this decomposition as an intermediate step is that wavelet denoising techniques could be applied without the usual computation cost of obtaining the decomposition of the wave-front. The proposed technique is illustrated with two examples and a discussion on sensor model errors. The reconstruction has been shown to be accurate despite relatively large noise signals (e.g., -20.3 dB error from 6 dB SNR for the 4-megapixel photograph). Results indicate that the proposed technique is a computationally efficient and accurate technique for wave-front and/or image reconstruction from Hudgin and Fried sensor models.

APPENDIX

The proof for how the gradient data can be transformed into the Haar decomposition is entirely based on algebraic manipulation of the standard HWAF and HWSF. The approach of the following algebra is to move the high pass filtering step that occurs at the end of the standard HWAF to the beginning via the noble identities. The model of a gradient sensor includes these highpass filters, so once the highpass filter is the first step of the filterbank it is trivial to move such filters out of the filterbank and into the sensor model.

The main steps of developing (15)–(27) from (11)–(14) are given in this section.

HL and LH quadrants: (15) and (16) follow directly from (12) and (13) for $m = 1$ and the definitions of ${}^M\tilde{X}$ and ${}^M\tilde{Y}$ given by (9) and (10).

LL quadrant: To derive (19), first (12) is factored to obtain an expression for ${}^{M-m}_{\text{LH}}\tilde{\Phi}$ which involves the available gradient data ${}^M\tilde{Y}$ instead of the image data ${}^M\Phi$ as in (A.1), shown at the bottom of the next page. The use of square brackets is to help indicate how the algebraic expansion in the second line relates to the first line. These brackets are dropped for the reordering in the

third line and finally ${}^M\Phi H_L(z_h)H_H(z_v)$ is directly replaced by ${}^M\tilde{Y}$ through the use of (10). The ${}^{M-m}\tilde{\Phi}_{\text{HL}}$ and ${}^{M-m}\tilde{\Phi}_{\text{HH}}$ terms are factored in similar ways [see (A.1), shown at the bottom of the page]. From the above nonrecursive equation and the definition of ${}^{k-1}\tilde{Y}$ in (17), the recursive (19) can be obtained using (A.2), shown at the bottom of the page.

Starting from (A.1) in the first line of (A.2), shown at the bottom of the page, the low-pass filters are factored out of the product operators in the second line. In the third line, the order of down-sampling is adjusted, which modifies the initial and final values of the product indices. In the fourth line, ${}^{M-1}\tilde{Y}$ is substituted using (17) which leads to an equation which is the same as the first line of (A.2) with $m \rightarrow m-1$ and $M \rightarrow M-1$. Repeating this circular process leads to the last line of (A.2) which after the substitution $m = M - k + 2$ becomes (19).

This shows that for the computation of ${}^{M-2}\tilde{\Phi}_{\text{LH}}$, ${}^{M-1}\tilde{Y}$ is computed first by filtering ${}^M\tilde{Y}$ and then this data is down-sampled to produce ${}^{M-2}\tilde{\Phi}_{\text{LH}}$. In the next iteration, the computation of ${}^{M-3}\tilde{\Phi}_{\text{LH}}$ can start with ${}^{M-1}\tilde{Y}$ which is available from the previous step, rather than begin with ${}^M\tilde{Y}$.

The derivation of (20) can be carried out in a similar way. From (13) and the definition of ${}^M\tilde{X}$, it follows that [see (A.3), shown at the bottom of the page], which, using the definition of ${}^{k-1}\tilde{X}$ in (18), leads to (20) in a similar way as with (19) from (A.2). Then (21) can be obtained by developing a nonrecursive form of (14) which involves the available gradient data ${}^M\tilde{X}$ instead of the image data ${}^M\Phi$ [see (A.4), shown at the bottom of the next page], and use the approach in (A.2) to obtain the recursive (21).

HH quadrant: To obtain the equations for the HH quadrant,

$$\begin{aligned}
 {}^{M-m}\tilde{\Phi}_{\text{LH}} &= \downarrow_{2^m} \left\{ {}^M\Phi \left[H_H \left(z_v^{2^{m-1}} \right) \right] \left[\prod_{k=0}^{m-1} H_L \left(z_h^{2^k} \right) \right] \prod_{k=0}^{m-2} H_L \left(z_v^{2^k} \right) \right\} \\
 &= \downarrow_{2^m} \left\{ {}^M\Phi \left[\sqrt{2}^{m-1} H_H(z_v) \prod_{k=0}^{m-2} H_L \left(z_v^{2^k} \right) \right] \cdots \right\} \\
 &\quad \left\{ \cdots \left[H_L(z_h) \prod_{k=1}^{m-1} H_L \left(z_h^{2^k} \right) \right] \prod_{k=0}^{m-2} H_L \left(z_v^{2^k} \right) \right\} \\
 &= \sqrt{2}^{m-1} \downarrow_{2^m} \left\{ {}^M\Phi H_L(z_h) H_H(z_v) \cdots \right\} \\
 &\quad \left\{ \cdots \prod_{k=1}^{m-1} H_L \left(z_h^{2^k} \right) \prod_{k=0}^{m-2} H_L^2 \left(z_v^{2^k} \right) \right\} \\
 &= \sqrt{2}^{m-1} \downarrow_{2^m} \left\{ {}^M\tilde{Y} \prod_{k=1}^{m-1} H_L \left(z_h^{2^k} \right) \prod_{k=0}^{m-2} H_L^2 \left(z_v^{2^k} \right) \right\}
 \end{aligned} \tag{A.1}$$

$$\begin{aligned}
 {}^{M-m}\tilde{\Phi}_{\text{LH}} &= \downarrow_{2^m} \left\{ {}^M\tilde{Y} \sqrt{2}^{m-1} \prod_{k=1}^{m-1} H_L \left(z_h^{2^k} \right) \prod_{k=0}^{m-2} H_L^2 \left(z_v^{2^k} \right) \right\} \\
 &= \downarrow_{2^{m-1}} \left\{ \downarrow_2 \left\{ {}^M\tilde{Y} \sqrt{2}^{m-1} H_L \left(z_h^2 \right) H_L^2 \left(z_v^2 \right) \cdots \right\} \right\} \\
 &\quad \left\{ \cdots \prod_{k=2}^{m-1} H_L \left(z_h^{2^k} \right) \prod_{k=1}^{m-2} H_L^2 \left(z_v^{2^k} \right) \right\} \\
 &= \downarrow_{2^{m-1}} \left\{ \downarrow_2 \left\{ {}^M\tilde{Y} \sqrt{2} H_L \left(z_h^2 \right) H_L^2 \left(z_v^2 \right) \right\} \cdots \right\} \\
 &\quad \left\{ \cdots \sqrt{2}^{m-2} \prod_{k=1}^{m-2} H_L \left(z_h^{2^k} \right) \prod_{k=0}^{m-3} H_L^2 \left(z_v^{2^k} \right) \right\} \\
 &= \downarrow_{2^{m-1}} \left\{ {}^{M-1}\tilde{Y}(z) \sqrt{2}^{m-2} \prod_{k=1}^{m-2} H_L \left(z_h^{2^k} \right) \prod_{k=0}^{m-3} H_L^2 \left(z_v^{2^k} \right) \right\} \\
 &\quad \vdots \\
 &= \downarrow_2 \left\{ {}^{M-m+1}\tilde{Y}(z) \right\}.
 \end{aligned} \tag{A.2}$$

$$\begin{aligned}
 {}^{M-m}\tilde{\Phi}_{\text{HL}} &= \downarrow_{2^m} \left\{ {}^M\Phi H_H \left(z_h^{2^{m-1}} \right) \prod_{k=0}^{m-2} H_L \left(z_h^{2^k} \right) \prod_{k=0}^{m-1} H_L \left(z_v^{2^k} \right) \right\} \\
 &= \downarrow_{2^m} \left\{ {}^M\Phi \sqrt{2}^{m-1} H_H(z_h) \prod_{k=0}^{m-2} H_L \left(z_h^{2^k} \right) \cdots \right\} \\
 &\quad \left\{ \cdots \prod_{k=0}^{m-2} H_L \left(z_h^{2^k} \right) H_L(z_v) \prod_{k=1}^{m-1} H_L \left(z_v^{2^k} \right) \right\} \\
 &= \sqrt{2}^{m-1} \downarrow_{2^m} \left\{ {}^M\tilde{X} \prod_{k=0}^{m-2} H_L^2 \left(z_h^{2^k} \right) \prod_{k=1}^{m-1} H_L \left(z_v^{2^k} \right) \right\}
 \end{aligned} \tag{A.3}$$

Φ_{HH}^{M-1} is decomposed with an M-1-stage HWAF to the form shown in Fig. 6. This implies that Φ_{LL}^{M-m} is obtained by applying (11) to Φ_{HH}^{M-1} . Then Φ_{HH}^{M-1} is substituted in this expression using (14) and after changing the order of down-sampling one obtains (A.5), shown at the bottom of the page.

Equations (A.6)–(A.8), shown at the bottom of the page, are obtained following similar operations as in (A.5). From (A.6) to (A.8), (A.9)–(A.11) follow, shown at the bottom of the page, by substituting (12) to (14) in the same manner as in (A.1),

(A.3), and (A.4): The recursive form of (23) to (27) follows from (A.9)–(A.11) in a similar way as obtaining (20) from (A.2).

ACKNOWLEDGMENT

The use of the wave-front simulation software package developed by Dr. R. Conan and the helpful suggestions and comments by the reviewers are gratefully acknowledged.

$$\begin{aligned}
 \Phi_{HH}^{M-m} &= \downarrow_{2^m} \left\{ M \Phi H_H(z_h^{2^{m-1}}) H_H(z_v^{2^{m-1}}) \prod_{k=0}^{m-2} H_L(z_h^{2^k}) \prod_{k=0}^{m-2} H_L(z_v^{2^k}) \right\} \\
 &= \downarrow_{2^m} \left\{ \begin{aligned} &M \Phi \sqrt{2}^{m-1} H_H(z_h) \prod_{k=0}^{m-2} H_L(z_h^{2^k}) \cdots \\ &\cdots \prod_{k=0}^{m-2} H_L(z_h^{2^k}) H_H(z_v^{2^{m-1}}) H_L(z_v) \prod_{k=1}^{m-2} H_L(z_v^{2^k}) \end{aligned} \right\} \\
 &= \sqrt{2}^{m-1} \downarrow_{2^m} \left\{ M \tilde{X} \prod_{k=0}^{m-2} H_L^2(z_h^{2^k}) H_H(z_v^{2^{m-1}}) \prod_{k=1}^{m-2} H_L(z_v^{2^k}) \right\} \quad (A.4)
 \end{aligned}$$

$$\begin{aligned}
 \Phi_{LL}^{M-m} &= \downarrow_{2^{m-1}} \left\{ \Phi_{HH}^{M-1} \prod_{k=0}^{m-2} H_L(z_h^{2^k}) \prod_{k=0}^{m-2} H_L(z_v^{2^k}) \right\} \\
 &= \downarrow_{2^{m-1}} \left\{ \begin{aligned} &\downarrow_2 \{ M \Phi H_H(z_h) H_H(z_v) \} \cdots \\ &\cdots \prod_{k=0}^{m-2} H_L(z_h^{2^k}) \prod_{k=0}^{m-2} H_L(z_v^{2^k}) \end{aligned} \right\} \\
 &= \downarrow_{2^m} \left\{ M \Phi H_H(z_h) H_H(z_v) \prod_{k=1}^{m-1} H_L(z_h^{2^k}) \prod_{k=1}^{m-1} H_L(z_v^{2^k}) \right\} \quad (A.5)
 \end{aligned}$$

$$\Phi_{LH}^{M-m} = \downarrow_{2^m} \left\{ \begin{aligned} &M \Phi H_H(z_h) H_H(z_v) H_H(z_h^{2^{m-1}}) \cdots \\ &\cdots \prod_{k=1}^{m-1} H_L(z_h^{2^k}) \prod_{k=1}^{m-2} H_L(z_v^{2^k}) \end{aligned} \right\} \quad (A.6)$$

$$\Phi_{HL}^{M-m} = \downarrow_{2^m} \left\{ \begin{aligned} &M \Phi H_H(z_h) H_H(z_v) H_H(z_h^{2^{m-1}}) \cdots \\ &\cdots \prod_{k=1}^{m-2} H_L(z_h^{2^k}) \prod_{k=1}^{m-1} H_L(z_v^{2^k}) \end{aligned} \right\} \quad (A.7)$$

$$\Phi_{HH}^{M-m} = \downarrow_{2^m} \left\{ \begin{aligned} &M \Phi H_H(z_h) H_H(z_v) H_H(z_h^{2^{m-1}}) \cdots \\ &\cdots H_H(z_v^{2^{m-1}}) \prod_{k=1}^{m-2} H_L(z_h^{2^k}) \prod_{k=1}^{m-2} H_L(z_v^{2^k}) \end{aligned} \right\} \quad (A.8)$$

$$\Phi_{LH}^{M-m} = \downarrow_{2^m} \left\{ M \tilde{X} H_H^2(z_v) \sqrt{2}^{m-1} \prod_{k=1}^{m-1} H_L(z_h^{2^k}) \prod_{k=1}^{m-2} H_L^2(z_v^{2^k}) \right\} \quad (A.9)$$

$$\Phi_{HL}^{M-m} = \downarrow_{2^m} \left\{ M \tilde{Y} H_H^2(z_h) \sqrt{2}^{m-1} \prod_{k=1}^{m-2} H_L^2(z_h^{2^k}) \prod_{k=1}^{m-1} H_L(z_v^{2^k}) \right\} \quad (A.10)$$

$$\begin{aligned}
 \Phi_{HH}^{M-m} &= \downarrow_{2^m} \left\{ \begin{aligned} &M \tilde{X} H_H(z_h^{2^{m-1}}) H_H^2(z_v) \cdots \\ &\cdots \sqrt{2}^{m-1} \prod_{k=1}^{m-2} H_L(z_h^{2^k}) \prod_{k=1}^{m-2} H_L^2(z_v^{2^k}) \end{aligned} \right\} \\
 &= \downarrow_{2^m} \left\{ \begin{aligned} &M \tilde{Y} H_H^2(z_h) H_H(z_v^{2^{m-1}}) \cdots \\ &\cdots \sqrt{2}^{m-1} \prod_{k=1}^{m-2} H_L^2(z_h^{2^k}) \prod_{k=1}^{m-2} H_L(z_v^{2^k}) \end{aligned} \right\}. \quad (A.11)
 \end{aligned}$$

REFERENCES

- [1] R. K. Tyson, *Introduction to Adaptive Optics*. Bellingham, WA: SPIE Press, 2000.
- [2] J. J. Widiker, S. R. Harris, and B. D. Duncan, "High-speed Shack-Hartmann wavefront sensor design with commercial off-the-shelf optics," *Appl. Opt.*, vol. 45, no. 2, pp. 383–395, Jan. 2006, Opt. Soc. Am..
- [3] C. R. Vogel and Q. Yang, "Multigrid algorithm for least-squares wavefront reconstruction," *Appl. Opt.*, vol. 45, no. 4, pp. 705–715, Feb. 2006.
- [4] B. L. Ellerbroek, "Efficient computation of minimum-variance wavefront reconstructors with sparse matrix techniques," *J. Opt. Soc. Amer. A*, vol. 19, no. 9, pp. 1803–1816, Sep. 2002.
- [5] D. L. Fried, "Least-square fitting a wave-front distortion estimate to an array of phase-difference measurements," *J. Opt. Soc. Amer.*, vol. 67, pp. 370–375, Mar. 1977.
- [6] R. Hudgin, "Wave-front reconstruction for compensated imaging," *J. Opt. Soc. Amer.*, vol. 67, pp. 375–378, Mar. 1977.
- [7] F. U. Dowl, J. M. Brase, S. S. Olivier, and C. A. Thompson, "Fast Fourier and wavelet transforms for wavefront reconstruction in adaptive optics," *Proc. SPIE*, vol. 4124, pp. 118–127, 2000.
- [8] P. Kovsi, "Shapelets correlated with surface normals produce surfaces," in *Proc. 10th IEEE Int. Conf. Computer Vision*, 2005, #1550-5499/05.
- [9] L. A. Poyneer, D. T. Gavel, and J. M. Brase, "Fast wavefront reconstruction in large adaptive optics systems with the Fourier transform," *J. Opt. Soc. Amer. A*, vol. 18, pp. 2100–2111, Oct. 2002.
- [10] K. Freischlad and C. Koliopoulos, "Modal estimation of a wave-front from difference measurements using the discrete Fourier transform," *J. Opt. Soc. Amer. A*, vol. 3, pp. 1852–1861, Nov. 1986.
- [11] L. A. Poyneer, B. A. Macintosh, and J.-P. Véran, "Fourier-transform wavefront control with adaptive prediction of the atmosphere," *J. Opt. Soc. Amer. A*, vol. 24, no. 9, pp. 2645–2660, Sept. 2007.
- [12] P. D. Kovsi, MATLAB and Octave Functions for Computer Vision and Image Processing Sch. Comput. Sci. & Software Eng., Univ. Western Australia, Perth [Online]. Available: <http://www.csse.uwa.edu.au/~pk/research/matlabfns>
- [13] A. Talmi and E. N. Ribak, "Wavefront reconstruction from its gradients," *J. Opt. Soc. Amer. A*, vol. 23, no. 2, pp. 288–297, Feb. 2006.
- [14] L. Gilles, B. Ellerbroek, and C. Vogel, "Multigrid preconditioned conjugate-gradient method for large-scale wave-front reconstruction," *J. Opt. Soc. Amer. A*, vol. 19, pp. 1817–1822, Sept. 2002.
- [15] L. Gilles, "Order-N sparse minimum-variance open-loop reconstructor for extreme adaptive optics," *Opt. Lett.*, vol. 28, no. 20, pp. 1927–1929, Oct. 2003.
- [16] J. Tumblin, A. Agrawal, and R. Raskar, "Why I want a gradient camera," in *Proc. IEEE Computer Society Conf. Computer Vision and Pattern Recognition (CVPR 2005)*, 2005, vol. 1, pp. 103–110.
- [17] R. J. Noll, "Zernike polynomials and atmospheric turbulence," *J. Opt. Soc. Amer.*, vol. 66, no. 3, pp. 207–211, Mar. 1976.
- [18] M. Vetterli and J. Kovacevic, *Wavelets and Subband Coding*. Upper Saddle River, NJ: Prentice-Hall, 1995, ch. 6.
- [19] D. T. Gavel, P. L. Wizinowich and D. Bonaccini, Eds., "Suppressing anomalous localized waffle behavior in least-squares wavefront reconstructors," in *Proc. SPIE*, Feb. 2003, vol. 4839, pp. 972–980, Adaptive Optical System Technologies II.
- [20] R. Conan *et al.*, "Optical parameters relevant for High Angular Resolution at Paranal from GSM instrument and surface layer contribution," *Astrophys. Suppl. Ser.*, vol. 144, pp. 39–44, May 2000.
- [21] T. Nakajima, "Signal-to-noise ratio of the bispectral analysis of speckle interferometry," *J. Opt. Soc. Amer. A*, vol. 5, p. 1477, 1988.
- [22] C. Roddier and F. Roddier, "Wave-front reconstruction from defocused images and the testing of ground-based optical telescopes," *J. Opt. Soc. Amer. A*, vol. 10, no. 11, pp. 2277–2287, Nov. 1993.
- [23] D. L. Donoho, "De-noising by soft thresholding," *IEEE Trans. Inform. Theory*, vol. 41, no. 5, pp. 613–627, May 1995.
- [24] E. D. Kolaczky, "Methods for analyzing certain signals and images in astronomy using Haar wavelets," in *Conf. Rec. 31st Asilomar Conf. Signals, Systems & Computers*, Nov. 1997, vol. 1, pp. 80–84.



Peter J. Hampton received the B.Eng. degree in electrical engineering (with distinction) in 2002 and the M.A.Sc. degree in 2006 in design and implementation of type 1 and type 2 closed-loop control systems on an adaptive optics test bench, both from the University of Victoria, Victoria, BC, Canada.

He is currently with the LACIR Adaptive Optics Laboratory, University of Victoria. His research interests include wavelet-based phase screen reconstruction, as well as the closed-loop control of multiple deformable mirrors in woofer-tweeter configurations.

Dr. Hampton received the Department of Electrical and Computer Engineering Excellence Recruitment Award and was also awarded a Fellowship in 2003 from the University of Victoria.



Pan Agathoklis received the Dipl. Ing. degree in electrical engineering and the Dr.Sc.Tech. degree from the Swiss Federal Institute of Technology, Zurich, Switzerland, in 1975 and 1980, respectively.

From 1981 to 1983, he was with the University of Calgary, Calgary, AB, Canada, as a Post-Doctoral Fellow and part-time Instructor. Since 1983, he has been with the Department of Electrical and Computer Engineering, University of Victoria, Victoria, BC, Canada, where he is currently a Professor. His fields of interest are in digital signal processing and its applications in control systems and communications.

Dr. Agathoklis received a NSERC University Research Fellowship (1984–1986) and Visiting Fellowships from the Swiss Federal Institute of Technology (1982, 1984, 1986, and 1993), from the Australian National University (1987), and the University of Perth, Perth, Western Australia (1997 and 2000). He was an Associate Editor for the IEEE TRANSACTIONS ON CIRCUITS AND SYSTEMS during 1990–1993. He has been a member of the Technical Program Committee of many international conferences and has served as the Technical Program Chair of the 1991 IEEE Pacific Rim Conference on Communications, Computers and Signal Processing and the 1998 IEEE Symposium on Advances in Digital Filtering and Signal Processing.



Colin Bradley received the B.A.Sc. degree in engineering physics from the University of British Columbia, Vancouver, BC, Canada, in 1985, the M.Sc. degree in electrical and electronic engineering from Heriot-Watt University, Edinburgh, Scotland, in 1987, and the Ph.D. degree in mechanical engineering from the University of Victoria, Victoria, BC, Canada, in 1992.

He is currently a Professor in the Department of Mechanical Engineering, University of Victoria, and has held the following positions and awards: Canada Research Chair in Design and Computational Modeling (2002–2007); Fellow of the Advanced Systems Institute of British Columbia (1993–2003); and Senior Research Fellow, National University of Singapore (1997–1999). His research focuses on adaptive optics, instrumentation for astronomy, deformable mirror technology; and implementing adaptive optics test benches.

Dr. Bradley is a member of the Optical Society of America and the International Society for Optical Engineering.